Symmetry breaking via alloy disorder to explain radiative Auger transitions in self-assembled quantum dots

Krzysztof Gawarecki [1,*] Clemens Spinnler [2] Liang Zhai [2] Giang N. Nguyen [2] Arne Ludwig [3]
Richard J. Warburton [2] Matthias C. Löbl [2,†] Doris E. Reiter [4,5] and Paweł Machnikowski [1]

[1]*Institute of Theoretical Physics, Wrocław University of Science and Technology, 50-370 Wrocław, Poland*
[2]*Department of Physics, University of Basel, Klingelbergstrasse 82, 4056 Basel, Switzerland*
[3]*Lehrstuhl für Angewandte Festkörperphysik, Ruhr-Universität Bochum, 44780 Bochum, Germany*
[4]*Condensed Matter Theory, TU Dortmund, 44221 Dortmund, Germany*
[5]*Institut für Festkörpertheorie, Universität Münster, 48149 Münster, Germany*

The optical spectrum of a quantum dot is typically dominated by the fundamental transition between the lowest-energy configurations. However, the radiative Auger process can result in additional redshifted emission lines. The origin of these lines is a combination of Coulomb interaction and symmetry breaking in the quantum dot. In this paper, we present measurements of such radiative Auger lines for a range of InGaAs/GaAs self-assembled quantum dots. We account for the Auger lines with a tight-binding model with a configuration interaction including symmetry breaking via alloy disorder. We show that the model accounts for the intensities of the Auger lines and the changes from quantum dot to quantum dot. We relate our findings to group theory explaining how the reduction in symmetry caused by alloy disorder is essential for the appearance of the radiative Auger lines.

I. INTRODUCTION

A self-assembled quantum dot (QD) can often be treated as a few-level system, in the simplest case as a two-level system, with discrete transition lines in the optical spectrum. Most pronounced is the fundamental transition associated with the recombination of the ground-state electron-hole pair. Such a transition can result in the emission of single photons to be used for quantum technologies [1–5].

Recently, additional spectral lines redshifted from the fundamental trion transition have been observed on a single negatively charged QD [6], as seen in Fig. 1. Remarkably, it is possible to drive these transitions with a resonant laser [7]. Similar features occur for positively charged QDs [8]. In a singly charged QD, the fundamental transition is associated with an electron-hole recombination that originates from the lowest-energy three-particle (trion) state and leaves the additional ("spectator") single electron or hole in its ground state. The additional lines stem from radiative Auger transitions mediated by the Coulomb interaction [6]. In the radiative

Auger process the energy of the recombining electron-hole pair is partially transferred to an intraband electronic excitation, which promotes the resident carrier to an excited state and redshifts the photon emission. Analogous transitions have been observed in the x-ray spectra of atoms [9–12] and, more recently, in optical spectra of semiconductor nanostructures [13,14]. Note that this effect includes a photon and therefore differs from the Auger scattering between electrons only, typically resulting in electron ejection from the QD [15,16]. When explored in QDs, the radiative Auger lines can be used for characterization of otherwise-unreachable single-particle excitation energies and provide temporal characteristics of single-carrier relaxation [6,7].

To describe theoretically the radiative Auger transitions, models including higher excited QD states and the Coulomb mixing between these states need to be employed [17–20]. In a perfectly symmetric QD (and neglecting any symmetry breaking at the atomic level), most of these transitions would be forbidden by symmetry. Accordingly, in order to account for the radiative Auger lines, it is important to consider asymmetries and imperfections. In addition, some observed features are not straightforward to explain. In particular, the strength of the radiative Auger lines varies from QD to QD and may reach values on the order of one percent of the fundamental line [6]; yet the observed lines do not show spin-related Zeeman splittings in a magnetic field, indicating a unique final spin state.

In this paper, we provide a thorough understanding of the radiative Auger process in InGaAs/GaAs QDs, including the above-mentioned peculiarities. We consider measurements on four QDs and model them using a tight-binding model. We

---

*Krzysztof.Gawarecki@pwr.edu.pl

†Present address: Center for Hybrid Quantum Networks (Hy-Q), The Niels Bohr Institute, University of Copenhagen, DK-2100 Copenhagen, Denmark.

explain how symmetry breaking induced by alloy disorder is crucially related to the appearance of the Auger lines. Alloy disorder occurs on the atomistic level by random appearance of either Ga or In atoms on the cation lattice sites. On the mesoscopic level, the alloy disorder can be investigated systematically by introducing an In-rich cluster. A statistical analysis of the consequences of symmetry breaking on the atomistic level accounts for the relative line intensities as found in the experiment. We support our finding by classifying the symmetry breaking using group theory.

II. THE RADIATIVE AUGER TRANSITIONS

Before introducing the theoretical model, we briefly describe the experimental observation of the radiative Auger transitions in QDs and the mechanism underpinning it. In the simplest, highly symmetric single-particle model, one obtains a series of transitions between valence and conduction band. For each transition line the initial and final state belong to the same single-particle shell of the QD spectrum. Additionally, the created electron and hole have opposite projections of the envelope angular momentum, corresponding to null envelope angular momentum projection of the electron-hole pair [21]. The resulting shell structure of optical excitations, corresponding to the sequence of *s–s*, *p–p* etc. transitions, has indeed been observed experimentally [22,23].

The Coulomb interaction modifies this simple picture in several ways. It renormalizes the energy of the electron-hole pair (which becomes an exciton) and introduces energy shifts between transitions taking place in the presence of other carriers (biexciton or trion transitions) [24,25]. It splits the lines according to their spin configurations due to exchange interactions [26]. It also hybridizes two-particle configurations [27]. The latter effect has been demonstrated in a double-QD structure, where the symmetry is lowered by a lateral offset of the QDs. The configuration mixing may then involve two-particle states of different angular momentum projections, which is revealed in the optical spectra of the system [27]. The radiative Auger process is another consequence of the Coulomb interaction and reveals Coulomb-induced configuration mixing in a single QD.

The structures investigated here are InGaAs QDs grown in the Stranski-Krastanov mode using a flushing technique [28,29]. To control the charge state, the QDs are placed in an *n-i-p* diode with a tunnel barrier of 40 nm between QDs and an *n*-type (silicon doped) backgate. The spectrum of scattered light (resonance fluorescence) was recorded upon resonant excitation of a single negatively charged QD [6]. At nonzero magnetic fields a selected spin configuration of the trion was excited by appropriate tuning of the resonant excitation. All experiments are performed at 4.2 K using a dark-field microscope that can distinguish QD emission from backreflected laser light by a cross-polarization scheme. Details on fabrication and measurement of the QDs can be found in Ref. [6].

An example spectrum is shown in Fig. 1. Some general properties of the measured spectra can be described using the idealized diagrams shown in Fig. 2, where we characterize the initial and final states using the spin, band, and envelope angular momenta (despite the fact that in presence of spin-orbit interaction and symmetry breaking, they are not strictly good
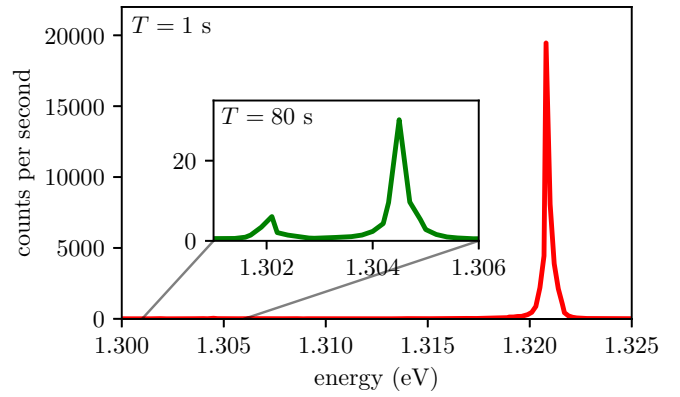

FIG. 1. Measured resonance fluorescence spectrum of an InGaAs/GaAs QD integrated for 1 s (red line, main panel) and 80 s (green line, inset). The spectrum corresponds to QD1 in Fig. 6.

quantum numbers). The first measurement of Fig. 1 (red line), performed using an integration time of 1 s, reveals a strong line at about 1.321 eV. It corresponds to the fundamental trion transition in which the "spectator" electron remains in its ground state. This situation is depicted schematically in Fig. 2, where the initial state is represented on the left, followed by the final state after optical emission [(a) for the fundamental transition]. Here the depicted levels and their labels (*s*, *p*, *d*) represent shells corresponding to the envelope states, while the Bloch wave functions are assumed *p* and *s* type for the valence and conduction bands, respectively. We stress that the fundamental transition is expected in the naive picture of uncorrelated interband transitions in a charged QD, where the
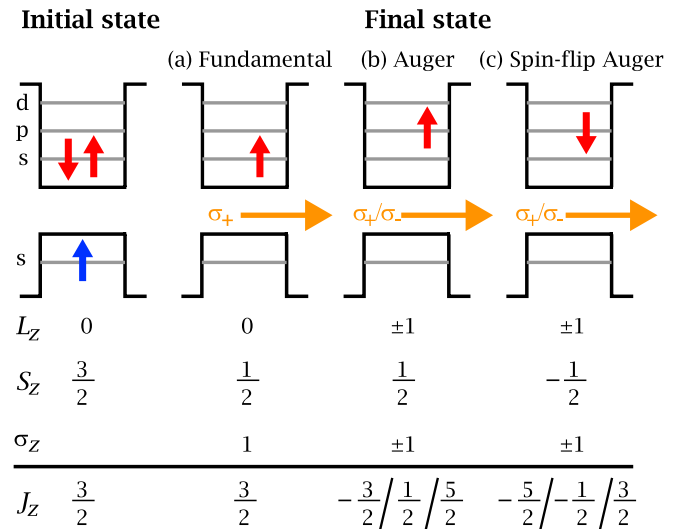

FIG. 2. Angular momentum in ground-state trion recombination. The initial state (left) decays into one of the final states, yielding either (a) the fundamental transition, (b) the Auger transition to the *p* shell, or (c) the spin-flip Auger transition to the *p* shell. Below each diagram we account for the angular momentum of the state, with L_z and S_z denoting the *z* projections of the envelope and band angular momenta of the carrier(s), respectively. σ_z represents the photon angular momentum ($\sigma_\pm$ denotes right and left circularly polarized photons), and J_z denotes the total angular momentum.

band angular momentum changes by 1 and the symmetry of the envelope function is conserved. Below the diagrammatic figures, we indicate the z projections of the envelope angular momentum (L_z), the band angular momentum (S_z), as well as the total angular momentum (J_z). Because the photon carries away an angular momentum of σ_z, the fundamental transition conserves the projection of the angular momentum on the symmetry axis and is therefore allowed.

While the strong fundamental transition line appears to be the only feature at short integration times, two additional lines appear at lower energies in the measurement performed with an extended integration time, plotted in the inset to Fig. 1. For this particular QD, the relative integrated intensity (compared to the fundamental transition) of these two lines is 0.34×10^{-3} and 1.2×10^{-3}, respectively. These lines are attributed to radiative Auger transitions. Crucially, we find that the overall intensities of the Auger lines as well as the intensity distribution between the two lines strongly varies from QD to QD.

In the idealized picture of the shells, the radiative Auger transition corresponds to the recombination of one electron-hole pair, while the remaining electron is promoted to the p shell. This is schematically shown in Figs. 2(b) and 2(c), where we indicate the two possible orientations of the electron spin in the final state. Note that apart from the spin degeneracy, the p shell in Fig. 2 is further twofold degenerate with respect to the envelope angular momentum, while in realistic QDs this degeneracy is lifted by anisotropy (caused by the inversion asymmetry of the underlying lattice, enhanced by anisotropy in the QD shape, atomic disorder, composition profile, strain, piezoelectric field, and nearby charge traps [14]) or an external magnetic field [30,31], yielding the two Auger lines visible in Fig. 1. At the bottom of Figs. 2(b) and 2(c) we list the values of the projection of the angular momentum in the initial state and in the final states. Note that the spin-flip Auger transition (c) can conserve angular momentum, while the transition (b) cannot.

To explain the observed features of the Auger lines, we develop a theoretical model that connects the observations to symmetry considerations.

III. THEORETICAL MODEL

A. QD shape

We assume an InGaAs QD in GaAs, which is elliptical in the lateral plane and capped in the z plane as shown in Fig. 3. Using a truncated elliptical Gaussian the surface of the dot is modelled by

$$S = w \exp\left\{ -\frac{l^2(x\cos\theta + y\sin\theta)^2 + (x\sin\theta - y\cos\theta)^2}{r_0^2} \right\},$$

where w is a parameter determining the slope, $2r_0$ is related to the lateral extension, while l describes the elongation in the direction given by θ. At the height h above the wetting layer the QD is truncated, which is consistent with the flushing step of the manufacturing process [28,32].

We take the following parameters: The slope is $w = 25a$ (where $a \approx 0.565$ nm is the GaAs lattice constant), $r_0 = 21a$, and the thickness of the wetting layer is chosen to be two monolayers corresponding to one lattice constant a. The size
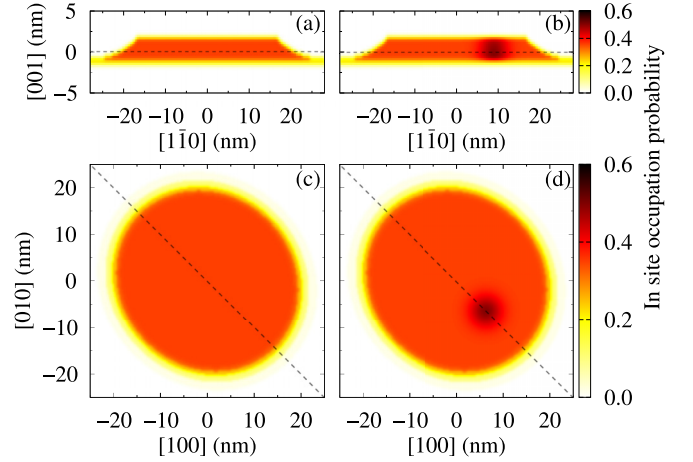

FIG. 3. Cross sections of compositions (In site occupation probability) for InGaAs/GaAs QDs without (a), (c) and with (b), (d) a composition cluster.

and shape of the QD is taken to be similar to the one described in Ref. [32]. Because InGaAs/GaAs QDs are often elongated in the $[1\bar{1}0]$ direction [33], we include such an effect in our model: we set the ellipticity to $l = (1.1)^{-1}$ and $\theta = -\pi/4$ corresponding to 10% elongation in the $[1\bar{1}0]$ direction. The composition is taken as $In_{0.35}Ga_{0.65}As$ in the QD and $In_{0.20}Ga_{0.80}As$ in the wetting layer.

B. Cluster

In order to study symmetry breaking systematically, we introduce symmetry breaking on the mesoscopic level by introducing a cluster with a higher In content than assumed elsewhere in the QD. The cluster is modeled by assuming a position-dependent composition profile of $In_{x(r)}Ga_{1-x(r)}As$ with $x(\boldsymbol{r}) = c_0 + c(\boldsymbol{r})$, where c_0 is the nominal indium content in the QD and

$$c(\boldsymbol{r}) = C_{cl}\exp\left\{ -\xi[(x-x_0)^2 + (y-y_0)^2 + (z-z_0)^2] \right\}$$

describes the locally increased indium content. Here (x_0, y_0, z_0) and ξ define the cluster position (with respect to the bottom of the wetting layer) and its spatial extension, respectively, while C_{cl} denotes the maximum additional In content. As the model is atomistic, the composition distribution $x(\boldsymbol{r})$ refers to the probability of finding an In atom at the given cation site. The cluster extends over a few lattice constants. An example is shown in Figs. 3(b) and 3(d). We note that such clusters are not unrealistic: in real nanostructures atoms of the same type may group together in some regions of the structure, and hence their positions are correlated to some degree. In fact, alloy intermixing effects were invoked to explain experimental data for the oscillator strength in InGaAs QDs [34].

As parameters we take $(x_0, y_0, z_0) = a(16/\sqrt{2}, 16/\sqrt{2}, 2)$, $\xi = 1/(6a)^2$. We consider a cluster with a higher In concentration, $C_{cl} = 0.15$. Note that this assumed maximum additional indium content is not very large compared to the overall nominal content of $c_0 = 0.35$. The composition distribution is processed by a Gaussian blur with a standard deviation of one GaAs lattice constant.

C. Atomistic disorder

Even in the absence of a cluster, the spatial "noise" in the underlying atomic arrangement (the alloy disorder) lowers the symmetry of the system on the atomistic level. In the tight-binding approach this effect is inherently present by the random appearance of Ga and In atoms (where the probability is related to the local composition) at the cation sites, and hence we refer to this as atomistic disorder. Such an approach neglects any correlation between the atomic positions, assuming a perfectly uncorrelated random alloy [35].

D. Coulomb interaction

To calculate the Coulomb-coupled states, we use the tight-binding $sp^3d^5s^*$ implementation described in Refs. [36,37] and utilize a configuration-interaction approach. The strain related to the lattice mismatch is accounted for within the valence-force-field model [38]. The resulting strain-induced piezoelectric potential is calculated including the polarization up to the second order in strain tensor elements using parameters from Ref. [39].

The wave functions of the single-particle states can be written as

$$|\Psi_i\rangle = \sum_n^{N_a} \sum_\alpha^{20} \varphi_{i,\alpha}(\boldsymbol{R}_n)|\boldsymbol{R}_n; \alpha\rangle,$$

where N_a is the total number of atoms in the system, $|\boldsymbol{R}_n; \alpha\rangle$ is an α atomic orbital on the site localized at $\boldsymbol{R}_n$, and $\varphi_{i,\alpha}(\boldsymbol{R}_n)$ are complex coefficients. As spin is taken into account, the basis for the $sp^3d^5s^*$ model contains 20 atomic states.

For the calculation of the Coulomb-coupled states, we change to the notation of second quantization, with $a_i^\dagger$ (a_i) and $h_i^\dagger$ (h_i) being the creation (annihilation) operators for the electron and hole single-particle states, respectively. With this we calculate the negative trion states $|X_\nu^-\rangle$ consisting of two electrons and one hole. The corresponding Hamiltonian reads [40,41]

$$H = \sum_i \epsilon_i^{(e)} a_i^\dagger a_i + \sum_j \epsilon_j^{(h)} h_j^\dagger h_j + \frac{1}{2} \sum_{ii'jj'} V_{ijj'i'}^{ee} a_i^\dagger a_j^\dagger a_{j'} a_{i'}$$
$$- \sum_{ii'jj'} V_{ijj'i'}^{eh} a_i^\dagger h_j^\dagger h_{j'} a_{i'} + \sum_{ii'jj'} V_{iji'j'}^{eh,exch} a_i^\dagger h_j^\dagger a_{i'} h_{j'}. \quad (1)$$

This Hamiltonian accounts for the electron/hole single-particle energies via $\epsilon_i^{(e/h)}$ [first two terms in Eq. (1)], as well as for the electron-electron and electron-hole Coulomb interaction (direct and exchange interaction) with the matrix elements given in Appendix. Because we only consider states with a single hole, the hole-hole Coulomb interaction does not contribute. We then use a configuration-interaction approach to obtain the Coulomb-coupled trion states.

The Hamiltonian is diagonalized in the basis of the lowest n_e electron and n_h hole states for expansion yielding the ground trion state $|X^-\rangle$ given by

$$|X^-\rangle = \sum_k^{n_h} \sum_{i,j}^{n_e} c_{kij} a_j^\dagger a_i^\dagger h_k^\dagger |\text{vac.}\rangle, \quad (2)$$

as well as the corresponding energy E_{X^-}. Here $|\text{vac.}\rangle$ is the vacuum state and c_{kij} are numerically found expansion coeffi-

cients with $i > j$. In addition, we consider the single-electron states $|l\rangle = a_l^+|\text{vac.}\rangle$ with the corresponding energies E_l.

E. Optical spectra

The radiative transitions in the many-particle system are described in the dipole approximation with the interband dipole moment operator [41]

$$\boldsymbol{D} = \sum_{i,j} \boldsymbol{d}_{ij} h_i a_j. \quad (3)$$

The matrix elements of the dipole moment between single-particle states are expressed in the tight-binding approach by

$$\boldsymbol{d}_{ij} \approx -e \sum_n^{N_a} \sum_\alpha^{20} \varphi_{i,\alpha}^{(v)*}(\boldsymbol{R}_n) \varphi_{j,\alpha}^{(c)}(\boldsymbol{R}_n) \boldsymbol{R}_n,$$

with the indices "v" denoting a state from the valence band and "c" a state from the conduction band. Here we neglect the contributions coming from the terms involving different nodes or orbitals, $\langle \boldsymbol{R}_m; \alpha|\boldsymbol{d}|\boldsymbol{R}_n; \beta\rangle \approx -e\boldsymbol{R}_n \delta_{mn}\delta_{\alpha\beta}$.

The emission line intensity I for the optical transition $|X^-\rangle \to |l\rangle$ is then given by

$$I_l = \frac{2m_0}{\hbar^2 e^2}(E_{X^-} - E_l) \sum_{\nu=x,y,z} |\langle l|D_\nu|X^-\rangle|^2, \quad (4)$$

where m_0 is the free electron mass, and the matrix element $\langle l|D_\nu|X^-\rangle$ is related to the expansion coefficients for trion states (see Appendix).

IV. RESULTS

We now use the tight-binding model to calculate the optical spectra in the vicinity of the fundamental transition line.

A. QD spectra with cluster

We start by considering a QD with a high In-composition cluster as shown in Fig. 4. We find a strong fundamental exciton transition line (red) at 1.334 meV. Redshifted by about 15 meV, we see a double-peak structure (green), which corresponds to the radiative Auger transition in which the remaining electron is promoted to the p shell. When presenting the computational results, we always sum over both spin configurations of the final state. Due to the in-plane asymmetry of the QD (including strain and piezoelectric field [30,42]), the p shell is split into the p_- and the p_+ line by about 5 meV in this calculation. In addition, about 30 meV below the fundamental line, we find three Auger lines (blue) belonging to the d-shell transitions with different oscillator strengths. The summed intensity of the p_+, p_- radiative Auger lines is about 10^{-2} of the main line. The particular in-plane anisotropy introduced by the cluster leads to a strong asymmetry in the p_+, p_- intensities. The in-plane anisotropy can be understood by looking at the wave functions of the electronic states as shown in the insets to Fig. 4. The wave functions become distorted towards the cluster, making them asymmetric. In particular, for the p-shell wave function, such asymmetry affects the p_- much more strongly than the p_+ wave function, thus leading to the different oscillator strengths of the p_- and p_+ radiative Auger lines.

The cluster, by controlling the symmetry breaking in a parametric way, enables us to understand how the p_- and
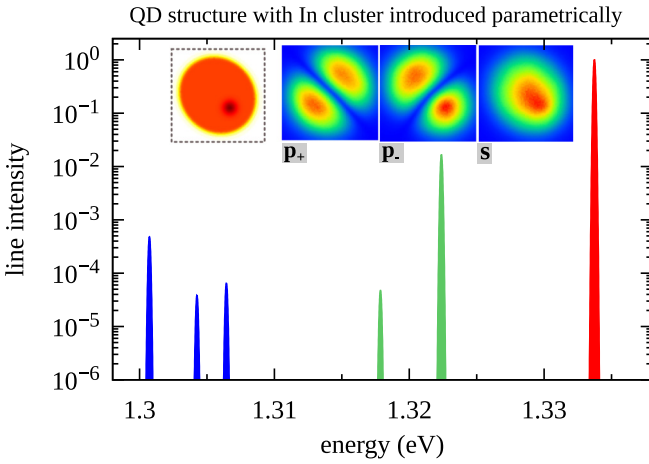
FIG. 4. Line intensity (logarithmic scale) of the transitions for a QD with a high In composition cluster as described in Sec. III A, normalized to the *s*-shell transition. The widths of the lines are artificial. A small magnetic field was added to lift the spin degeneracy (not visible, as the spin Zeeman splitting is smaller than the linewidths). The panels present probability densities of *s*- and *p*-type electron states in the (001) plane in the same crystallographic orientation as in Figs. 3(c) and 3(d).

p_+ radiative Auger lines are so sensitive to the details of the *p*-shell wave functions.

B. QD spectra with only atomic disorder

Theoretical results for the same QD parameters (size, alloy concentration) but without a cluster are presented in Table I for ten randomly chosen alloy configurations, S1–S10. We define ΔE_p as the energy difference between the p_- and p_+ lines, and p_- (p_+) as the integrated intensity of the p_--line (p_+-line) relative to the fundamental line. As metrics for the total Auger intensity and the asymmetry in the spectrum, we take $\Sigma_p = p_+ + p_-$ and p_-/Σ_p, respectively.

TABLE I. Calculated energy difference ΔE_p between the p_+ and p_- Auger lines, their intensities relative to the fundamental transition p_- and p_+, as well as the sum $\Sigma_p = p_- + p_+$ and the ratio p_-/Σ_p for ten randomly chosen alloy configurations. The results are for vanishing magnetic field. Bottom rows display the calculated mean and standard derivation (SD) values.

	ΔE_p (meV)	p_- (10^{-3})	p_+ (10^{-3})	Σ_p (10^{-3})	p_-/Σ_p
S1	2.5	0.96	0.48	1.44	0.66
S2	2.1	0.94	0.77	1.71	0.55
S3	0.9	0.07	1.75	1.82	0.04
S4	0.8	0.10	2.36	2.46	0.04
S5	2.2	0.09	0.22	0.31	0.29
S6	2.1	0.77	2.65	3.42	0.22
S7	2.3	3.07	0.07	3.14	0.98
S8	2.2	0.71	0.04	0.75	0.95
S9	3.4	0.52	0.08	0.60	0.87
S10	3.7	5.88	0.05	5.93	0.99
Mean	2.21	1.31	0.85	2.16	0.56
SD	0.91	1.82	1.02	1.68	0.39

TABLE II. Energy difference ΔE_p between the p_+ and p_- Auger lines, their intensities relative to the fundamental transition p_- and p_+, as well as the sum of the two intensities $\Sigma_p = p_+ + p_-$ and the ratio p_-/Σ_p at zero magnetic field for the four experimentally studied QDs (cf. Fig. 6). Bottom rows display the calculated mean and standard derivation (SD) values.

	ΔE_p (meV)	p_- (10^{-3})	p_+ (10^{-3})	Σ_p (10^{-3})	p_-/Σ_p
QD1	2.4	1.2	0.34	1.54	0.78
QD2	5.6	2.7	1.9	4.6	0.59
QD3	2.1	2.2	0.0	2.2	1.0
QD4	2.0	0.50	0.97	1.47	0.34
Mean	3.03	1.65	0.8	2.45	0.68
SD	1.73	0.99	0.83	1.47	0.28

The results in Table I show that both $\Sigma_p = p_+ + p_-$ and p_-/Σ_p fluctuate from alloy configuration to alloy configuration. This is clear evidence for the importance of atomic-scale disorder. The particular alloy configuration can have a significant effect on the p_- and p_+ wave functions. Based on the understanding gleaned with the cluster, this dependence leads to a strong dependence of the p_- and p_+ radiative Auger intensities on the alloy configuration. In other words, we deduce that even in the absence of a well-defined cluster, the absolute and relative intensities of the p_+, p_- radiative Auger lines are determined by the details of the atomic disorder.

C. Comparison of calculated and experimental QD spectra

Four QDs were measured in detail. All the metrics describing the radiative Auger lines vary from QD to QD, despite the fact that all three QDs are in the same sample and are therefore self-assembled under the same conditions (Table II). p_-/Σ_p is above 50% in three cases (QD1-QD3), below 50% in one (QD4).

In the theory (focusing on the results without a cluster), the radiative Auger parameters change from run to run. We compare the statistics (mean and standard deviation) of ΔE_p, Σ_p, and p_-/Σ_p between experiment and theory.

The theory accounts for the total intensity of the radiative Auger lines convincingly: the measured average of Σ_p is $(2.45 \pm 1.47) \cdot 10^{-3}$; the calculated average is $(2.16 \pm 1.68) \cdot 10^{-3}$. Without atomic-scale disorder, Σ_p is negligible. Furthermore, the standard deviations of Σ_p, experiment and theory, also match quite well. For the available data, the average p_-/Σ_p values, experiment and theory, also match. This is evidence that atomistic alloy disorder alone is sufficient to account for the in-plane anisotropy. Finally, there is a reasonable match in the average values of ΔE_p. This is a less powerful metric for the radiative Auger process: QD shape anisotropy has a strong effect on ΔE_p but not on Σ_p. The main point concerning ΔE_p is that alloy disorder results in significant changes from QD to QD, even for the same shape and alloy concentration.

We stress that both in the experiment and in the theory a wide range of Σ_p and ΔE_p values is observed for the radiative Auger lines. The overall agreement between the statistical properties of the experimental and theoretical data sets is very good. This quantitative agreement in the statistical properties
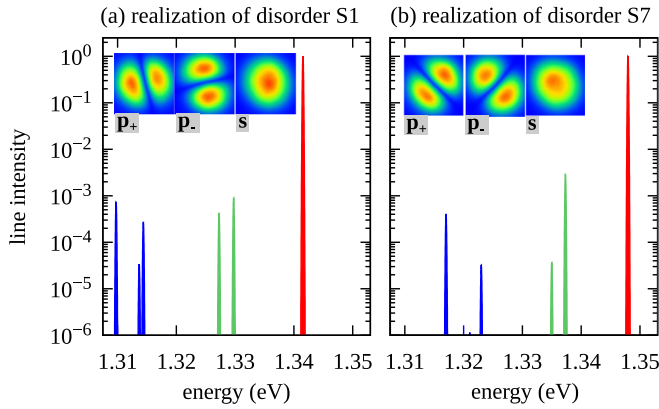
FIG. 5. Line intensity (logarithmic scale) of the transitions for two realizations of atomic disorder in QD as described in Sec. IV B, normalized to the *s*-shell transition. The widths of the lines are artificial. A small magnetic field was added to lift the spin degeneracy (not visible, as the spin Zeeman splitting is smaller than the widths of the lines). The panels present probability densities of *s*- and *p*-type electron states in the (001) plane in the same crystallographic orientation as in Figs. 3(c) and 3(d).

is compelling evidence that the theory isolates the correct source of symmetry breaking, namely, atomic-scale alloy disorder.

D. Spin-flip radiative Auger

The spin-flip Auger transition, represented in Fig. 2(c), may conserve the axial projection of the angular momentum upon transferring the angular momentum between the orbital and spin degrees of freedom. One could therefore

expect that this transition may be allowed in the presence of spin-orbit couplings. Our simulations show, however, that the spin-conserving processes [Fig. 2(b)] typically dominate for the *p*-shell Auger lines. We conclude, therefore, that spin-orbit effects are overwhelmed by the effects of symmetry breaking in the radiative Auger process. This also describes the experimental results for which no spin-flip radiative Auger lines could be observed with the present experiment.

E. Magnetic field dependence

Another interesting feature of the Auger lines is their dependence on an applied external magnetic field. Examples of the measured magnetic field dependence are shown in Figs. 6(a)–6(d) [6]. While the fundamental transition remains rather unchanged under the influence of a magnetic field, apart from a slight diamagnetic shift, the *p*-shell Auger lines show a typical orbital Zeeman splitting. In some cases an anticrossing with the *d*-shell Auger lines is observed [e.g., at a magnetic field of $B = 6$ T in Fig. 6(b)]. The overall behavior of the *p*-shell Auger lines is rather similar for QD1-4, with the main difference found in the relative line intensities as discussed in the previous section. However, the visibility of the *d* shell varies from QD to QD. This could be a consequence of the proximity of the continuum states in the wetting layer. It is known that the thickness of the wetting layer and hence the energetic separation between wetting layer and QD levels fluctuates [43].

In the theoretical modeling we include the interaction with the magnetic field in Faraday geometry in the tight-binding approach by the Peierls substitution and on-site Zeeman terms [44,45]. A detailed description of the model is given in Ref. [46]. The obtained spectra are shown in Fig. 6(e) for
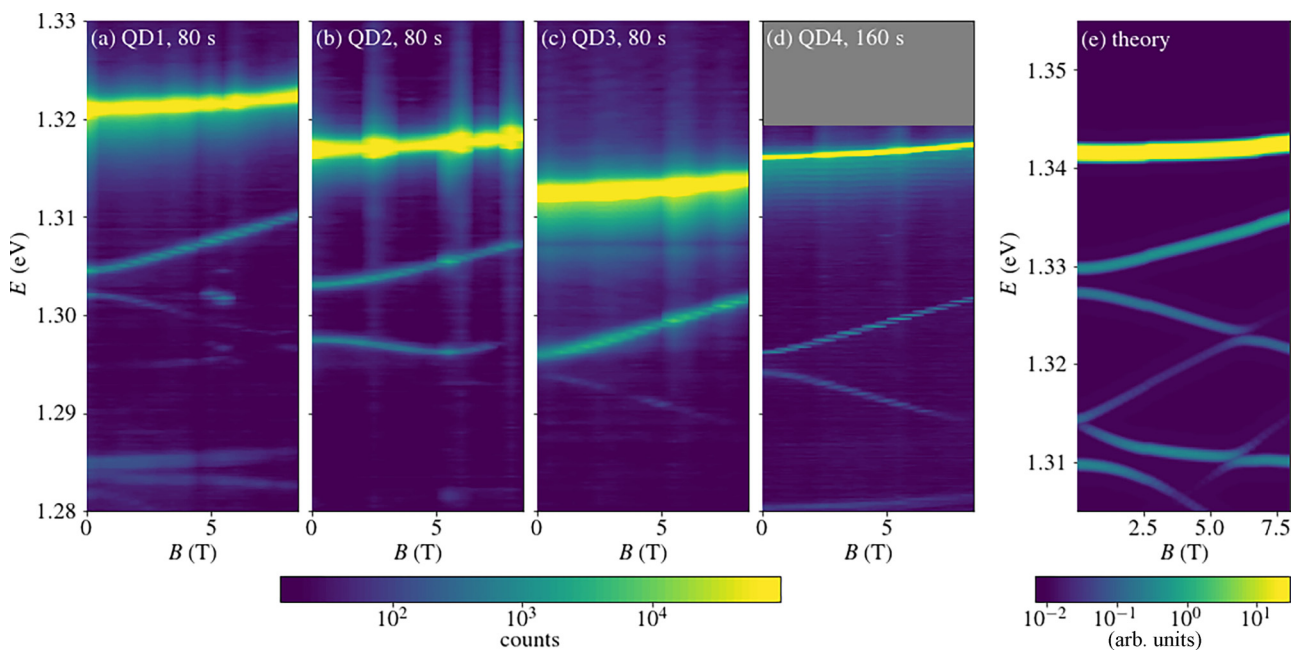

FIG. 6. (a)–(d) Experimentally measured spectra of four different QDs; (e) theoretically calculated spectrum of a QD (S1 alloy configuration) as a function of the external magnetic field. The color bar refers to the experimental plots (a)–(d) and shows the number of detection counts within the integration period indicated in each panel. In the theoretical data, the color is related to the intensity [Eq. (4)] with an artificial broadening. Both color bars use a logarithmic scale.

TABLE III. Character table of the irreducible representations of the C_{2v} and C_s point groups [47]. E is an identity element, σ are reflection planes described by the Miller indices, and C_2 is the rotation by π. Note that in the basis functions used here, in contrast to the other parts of the article, the x direction is [110] and y is [$\bar{1}$10].

C_{2v}	E	C_2	$\sigma_v(110)$	$\sigma_v(\bar{1}10)$	Basis functions
Γ_1	1	1	1	1	$1, z, x^2, y^2, z^2$
Γ_2	1	1	-1	-1	xy
Γ_3	1	-1	1	-1	y, yz
Γ_4	1	-1	-1	1	x, xz

C_s	E		$\sigma_v(110)$		Basis functions
Γ_1	1		1		$1, y, z$
Γ_2	1		-1		x

a QD with the S1 realization of atomic disorder. We find that the overall agreement with the experimental data is very good. In particular, the energetic behavior of the lines can be well reproduced, and we also find the anticrossing between the different shells. Throughout the considered magnetic field range, the p-shell Auger transitions are strongly dominated by the spin-conserving process [Fig. 2(b)].

V. GROUP-THEORETICAL CONSIDERATIONS

The appearance of the radiative Auger lines by symmetry breaking can be explained using group theory. While these arguments are not sufficient to predict the strength of the lines as obtained from the numerical calculation, they allow one to predict some qualitative properties of the Auger process for various system symmetries.

We focus initially on major symmetry breaking at the level of the QD shape, ignoring for the moment atomic disorder, band mixing, spin-orbit coupling, and the effect of a magnetic field. In such an approximation, the optical transitions take place only if the envelopes of the initial and the final state belong to the same irreducible representation of a given group. The participating states in the optical transition are the electron states $|l\rangle$ and the ground trion state $|X^-\rangle$, for which we investigate the representations linked to their envelopes. It is convenient to highlight the symmetry of the single-particle states $|l\rangle$ by using a shell-based notation, where we label the states with their approximate envelope type starting with $l = s$ followed by the lower and upper p-shell states, $l = p_-$ and p_+, and then the d-shell states.

The bare elliptical QD [Figs. 3(a) and 3(c)] is described by the C_{2v} group, which contains one operation of rotation and two reflection planes (see the character table, Table III). Due to its transformation rules, the electron ground state $|s\rangle$ belongs to the identity representation Γ_1. On the other hand, the first excited states $|p_-\rangle$ and $|p_+\rangle$ belong to Γ_3 and Γ_4, respectively [which can also be seen in the insets of Fig. 5(b)]. Being a ground state, $|X^-\rangle$ belongs to the Γ_1 representation. In consequence, the fundamental transition from $|X^-\rangle$ to the $|s\rangle$ electron state is allowed, while the Auger transitions to $|p_-\rangle$ and $|p_+\rangle$ are prohibited by group-theoretical arguments.

The symmetry can be reduced in a parametric way by adding a composition cluster to the QD [Figs. 3(b) and 3(d)]. The cluster reduces the symmetry to the C_s group, which

contains a reflection by a single plane (see the character Table III). As before, the trion $|X^-\rangle$ and the electron $|s\rangle$ states are linked to the identity representation Γ_1. However, due to the symmetry reduction by the cluster, $|p_-\rangle$ and $|p_+\rangle$ now belong to Γ_1 and Γ_2, respectively. In consequence, the Auger transition $|X^-\rangle \leftrightarrow |p_-\rangle$ is now allowed. This is in agreement with the observation of a large peak related to this process, as observed in the numerical simulations of Fig. 4. The symmetry reduction from C_{2v} to C_s was also shown to be crucial for optical activity of dark excitons in self-assembled QDs [48].

Even without a cluster, an InGaAs QD does not have C_{2v} symmetry: in an exact approach, the alloy disorder reduces the symmetry. All the considered systems have strictly C_1 symmetry, where all the states reside in the same representation. This is the origin of the p_- and p_+ Auger lines in the simulations of Fig. 5. In fact, this symmetry reduction allows even further Auger transitions.

VI. CONCLUSIONS

In conclusion, we have presented a tight-binding approach to model the radiative Auger lines as observed recently on semiconductor QDs. We were able to reproduce the line positions and their behavior in a magnetic field. We showed that in the presence of alloy disorder, the model explains the measured relative strength of the radiative Auger lines and the changes from QD to QD. Additionally, we linked the Auger lines to group-theoretical considerations. This highlights the importance of symmetry breaking below the C_{2v} point group that characterizes elliptical QDs on the mesoscopic level.

The overriding point is that the radiative Auger process is highly sensitive to symmetry breaking on the mesoscopic or atomic length scale, i.e., on length scales smaller than the QD dimensions. As such, radiative Auger can reveal information on morphological details of QDs. Furthermore, given that alloying is sufficient to deliver the required symmetry breaking, also other types of self-assembled QDs will show radiative Auger emission lines.

Note added in proof. Recently, we became aware of a paper by Jain *et al.* [49], where a mechanism of symmetry breaking by alloy disorder, similar to ours, was invoked in a different system of CdSe/CdS core-shell quantum dots to explain the nonradiative Auger effect (pure Coulomb scattering).

APPENDIX: MODEL IMPLEMENTATION

Here we present some additional details of our model complementing Sec. III, including explicit expressions for the Coulomb matrix elements. The piezoelectric potential $\Phi_p(\boldsymbol{r})$ [entering the Hamiltonian via $V_p(\boldsymbol{r}) = -e\Phi_p(\boldsymbol{r})$] is calculated by solving the Poisson-like equation [51]

$$-\epsilon_0 \nabla \cdot [\epsilon_r(\boldsymbol{r}) \nabla \Phi(\boldsymbol{r})] = -\nabla \cdot \boldsymbol{P}(\boldsymbol{r}), \tag{A1}$$

where ϵ_0 is the vacuum permittivity, $\epsilon_r(\boldsymbol{r})$ is the position-dependent relative permittivity, and $\boldsymbol{P}(\boldsymbol{r})$ is the polarization, which is calculated from the local strain tensor elements [39,52]:

$$\boldsymbol{P} = 2e_{14}\begin{pmatrix} \epsilon_{yz} \\ \epsilon_{xz} \\ \epsilon_{xy} \end{pmatrix} + 2B_{114}\begin{pmatrix} \epsilon_{xx}\epsilon_{yz} \\ \epsilon_{yy}\epsilon_{xz} \\ \epsilon_{zz}\epsilon_{xy} \end{pmatrix} + 4B_{156}\begin{pmatrix} \epsilon_{xz}\epsilon_{xy} \\ \epsilon_{yz}\epsilon_{xy} \\ \epsilon_{yz}\epsilon_{xz} \end{pmatrix}$$
$$+ 2B_{124}\begin{pmatrix} (\epsilon_{yy}+\epsilon_{zz})\epsilon_{yz} \\ (\epsilon_{xx}+\epsilon_{zz})\epsilon_{xz} \\ (\epsilon_{xx}+\epsilon_{yy})\epsilon_{xy} \end{pmatrix}.$$

The strain tensor elements at cations are calculated following Ref. [38], and at anions they are obtained by averaging the values from the neighboring cations. We take $\epsilon_r(\text{InAs}) = 14.6$ and $\epsilon_r(\text{GaAs}) = 12.4$ [53,54]. The values of e_{14}, B_{114}, B_{156}, and B_{124} are taken from Ref. [39]. We discretize Eq. (A1) using the finite-difference scheme for the atomistic grid [55]. For the anion at position $\boldsymbol{R}_i$, this gives

$$\sum_j^{\text{NN}(i)} [\epsilon_r(\boldsymbol{R}_i + \boldsymbol{d}_j) + \epsilon_r(\boldsymbol{R}_i)][\Phi_p(\boldsymbol{R}_i + \boldsymbol{d}_j) - \Phi_p(\boldsymbol{R}_i)]$$
$$= \frac{a}{4\epsilon_0}\{[P_x(\boldsymbol{R}_i + \boldsymbol{d}_1) - P_x(\boldsymbol{R}_i + \boldsymbol{d}_2) - P_x(\boldsymbol{R}_i + \boldsymbol{d}_3)$$
$$+ P_x(\boldsymbol{R}_i + \boldsymbol{d}_4)] + [P_y(\boldsymbol{R}_i + \boldsymbol{d}_1) - P_y(\boldsymbol{R}_i + \boldsymbol{d}_2)$$
$$+ P_y(\boldsymbol{R}_i + \boldsymbol{d}_3) - P_y(\boldsymbol{R}_i + \boldsymbol{d}_4)] + [P_z(\boldsymbol{R}_i + \boldsymbol{d}_1)$$
$$+ P_z(\boldsymbol{R}_i + \boldsymbol{d}_2) - P_z(\boldsymbol{R}_i + \boldsymbol{d}_3) - P_z(\boldsymbol{R}_i + \boldsymbol{d}_4)]\}, \tag{A2}$$

where $\text{NN}(i)$ denote the nearest neighbors of the ith atom. For the unstrained lattice, the positions of the surrounding cations are given by

$$\boldsymbol{d}_1 = \frac{a}{4}(1, 1, 1),$$
$$\boldsymbol{d}_2 = \frac{a}{4}(-1, -1, 1),$$
$$\boldsymbol{d}_3 = \frac{a}{4}(-1, 1, -1),$$
$$\boldsymbol{d}_4 = \frac{a}{4}(1, -1, -1).$$

In the case of the cation at $\boldsymbol{R}_i$, the discretization takes the form

$$\sum_j^{\text{NN}(i)} [\epsilon_r(\boldsymbol{R}_i - \boldsymbol{d}_j) + \epsilon_r(\boldsymbol{R}_i)][\Phi_p(\boldsymbol{R}_i - \boldsymbol{d}_j) - \Phi_p(\boldsymbol{R}_i)]$$
$$= -\frac{a}{4\epsilon_0}\{[P_x(\boldsymbol{R}_i - \boldsymbol{d}_1) - P_x(\boldsymbol{R}_i - \boldsymbol{d}_2) - P_x(\boldsymbol{R}_i - \boldsymbol{d}_3)$$
$$+ P_x(\boldsymbol{R}_i - \boldsymbol{d}_4)] + [P_y(\boldsymbol{R}_i - \boldsymbol{d}_1) - P_y(\boldsymbol{R}_i - \boldsymbol{d}_2)$$

$$+ P_y(\boldsymbol{R}_i - \boldsymbol{d}_3) - P_y(\boldsymbol{R}_i - \boldsymbol{d}_4)] + [P_z(\boldsymbol{R}_i - \boldsymbol{d}_1)$$
$$+ P_z(\boldsymbol{R}_i - \boldsymbol{d}_2) - P_z(\boldsymbol{R}_i - \boldsymbol{d}_3) - P_z(\boldsymbol{R}_i - \boldsymbol{d}_4)]\}. \tag{A3}$$

One should note that Eqs. (A2) and (A3) are derived for the unstrained zinc-blende lattice. We use this approach here with relaxed atomic positions. However, this approximation can be justified by the fact that strain is typically on the order of a few percent. The resulting set of linear equations is solved numerically using the library PETSC [56].

The starting point of further calculations is the single-particle wave functions $|\Psi_i\rangle$ as given in Sec. III D, which are superpositions of the electronic wave functions of the atoms in the system. In the next step, we use the configuration-interaction (CI) Hamiltonian as given in Eq. (1). The calculations were performed with the basis of $n_e = 20$ and $n_h = 20$. The valence-band wave functions were transformed to the hole picture via a time-reversal operation. The difference between the p-shell Auger intensities obtained with 12 and 20 basis states for the QD without cluster is up to 50%. On the other hand, with a high-In cluster, these results are much less affected (the difference is below 5% for the p_- emission line). In the tight-binding basis, the Coulomb matrix elements between a particle A and B are given by [40,41]

$$V_{ijj'i'}^{AB} \approx V_0 + \frac{|e|^2}{4\pi\epsilon_0\epsilon_r} \sum_{n,m\neq n}^{N_a} \sum_{\alpha,\beta}^{20}$$
$$\times \frac{\varphi_{i,\alpha}^{(A)*}(\boldsymbol{R}_n)\varphi_{j,\beta}^{(B)*}(\boldsymbol{R}_m)\varphi_{j',\beta}^{(B)}(\boldsymbol{R}_m)\varphi_{i',\alpha}^{(A)}(\boldsymbol{R}_n)}{|\boldsymbol{R}_n - \boldsymbol{R}_m|},$$
$$V_{iji'j'}^{AB,\text{exch}} \approx V_0^{\text{exch}} + \frac{|e|^2}{4\pi\epsilon_0\epsilon_r} \sum_{n,m\neq n}^{N_a} \sum_{\alpha,\beta}^{20}$$
$$\times \frac{\varphi_{i,\alpha}^{(A)*}(\boldsymbol{R}_n)\varphi_{j,\beta}^{(B)*}(\boldsymbol{R}_m)\varphi_{i',\beta}^{(A)}(\boldsymbol{R}_m)\varphi_{j',\alpha}^{(B)}(\boldsymbol{R}_n)}{|\boldsymbol{R}_n - \boldsymbol{R}_m|},$$

where we took the value for GaAs, $\epsilon_r = 12.4$. V_0 and V_0^{exch} account for the short-range on-site contributions, which we neglect here. Such elements could be calculated using the basis of atomic orbitals (e.g., the Slater orbitals) [41,57,58]. However, for direct-band-gap QDs, the on-site elements vanish much faster with an increasing QD size than the monopole-monopole long-range terms [59–61]. For the InAs QDs considered in Ref. [61], the on-site terms contributed only about 1% to the direct Coulomb attraction for the ground electron-hole states and 20% to the exchange-interaction-induced splitting. We calculate the two center contributions using the expansion according to the Fourier theorem,

$$\frac{1}{|\boldsymbol{R}_n - \boldsymbol{R}_m|} = \frac{1}{(2\pi)^3}\int \frac{4\pi}{q^2}e^{i\boldsymbol{q}(\boldsymbol{R}_n - \boldsymbol{R}_m)}\mathrm{d}\boldsymbol{q},$$

which allows us to write

$$V_{ijj'i'}^{AB} \approx \frac{|e|^2}{8\pi^3\epsilon_0\epsilon_r}\int \frac{F_{ii'}^{(AA)}(\boldsymbol{q})F_{j'j}^{(BB)*}(\boldsymbol{q})}{q^2}\mathrm{d}\boldsymbol{q},$$
$$V_{iji'j'}^{AB,\text{exch}} \approx \frac{|e|^2}{8\pi^3\epsilon_0\epsilon_r}\int \frac{F_{ij'}^{(AB)}(\boldsymbol{q})F_{i'j}^{(AB)*}(\boldsymbol{q})}{q^2}\mathrm{d}\boldsymbol{q},$$

where

$$F_{ij}^{(AB)}(\boldsymbol{q}) = \sum_n^{N_a} \sum_\alpha^{20} \varphi_{i,\alpha}^{(A)*}(\boldsymbol{R}_n)\varphi_{j,\alpha}^{(B)}(\boldsymbol{R}_n)e^{i\boldsymbol{q}\boldsymbol{R}_n},$$

which we calculated efficiently using the FINUFFT library [62–64]. To perform the calculations for $V_{ijj'i'}^{AB}$ and $V_{iji'j'}^{AB,\text{exch}}$, we use spherical coordinates where the $1/q^2$ singularity is removed by the Jacobian. We take the maximal value of q in the integration as π/a. We checked that the exchange-interaction terms have a relatively small impact on the considered p-shell Auger transitions. After the diagonalization in the basis of the n_e electron and n_h hole states, we obtain the energies E_{X^-}

and coefficients c_{kij} from which the trion ground state $|X^-\rangle$ is formed as described in Eq. (2).

The expansion coefficients of the Coulomb-coupled trion states, on the other hand, enter in the calculation of the matrix element of the transition operator $\mathbf{D}$ given in Eq. (3):

$$\langle l|\boldsymbol{D}|X^-\rangle = \langle\text{vac.}|a_l \sum_{i',j'} \boldsymbol{d}_{i'j'} \, h_{i'}a_{j'} \sum_{k,i,j} c_{kij}$$
$$\times a_j^\dagger a_i^\dagger h_k^\dagger|\text{vac.}\rangle$$
$$= \sum_{k,i,j} c_{kij}(\boldsymbol{d}_{ki}\delta_{lj} - \boldsymbol{d}_{kj}\delta_{li}),$$

where $i > j$.

[1] C. Santori, D. Fattal, J. Vuckovic, G. S. Solomon, and Y. Yamamoto, Indistinguishable photons from a single-photon device, Nature (London) **419**, 594 (2002).

[2] L. Schweickert, K. D. Jöns, K. D. Zeuner, S. F. Covre da Silva, H. Huang, T. Lettner, M. Reindl, J. Zichi, R. Trotta, A. Rastelli, and V. Zwiller, On-demand generation of background-free single photons from a solid-state source, Appl. Phys. Lett. **112**, 093106 (2018).

[3] B.-Y. Wang, E. V. Denning, U. M. Gür, C.-Y. Lu, and N. Gregersen, Micropillar single-photon source design for simultaneous near-unity efficiency and indistinguishability, Phys. Rev. B **102**, 125301 (2020).

[4] N. Tomm, A. Javadi, N. O. Antoniadis, D. Najer, M. C. Löbl, A. R. Korsch, R. Schott, S. R. Valentin, A. D. Wieck, A. Ludwig, and R. J. Warburton, A bright and fast source of coherent single photons, Nat. Nanotechnol. **16**, 399 (2021).

[5] L. Zhai, G. N. Nguyen, C. Spinnler, J. Ritzmann, M. C. Löbl, A. D. Wieck, A. Ludwig, A. Javadi, and R. J. Warburton, Quantum interference of identical photons from remote GaAs quantum dots, Nat. Nanotechnol. **17**, 829 (2022).

[6] M. C. Löbl, C. Spinnler, A. Javadi, L. Zhai, G. N. Nguyen, J. Ritzmann, L. Midolo, P. Lodahl, A. D. Wieck, A. Ludwig, and R. J. Warburton, Radiative Auger process in the single-photon limit, Nat. Nanotechnol. **15**, 558 (2020).

[7] C. Spinnler, L. Zhai, G. N. Nguyen, J. Ritzmann, A. D. Wieck, A. Ludwig, A. Javadi, D. E. Reiter, P. Machnikowski, R. J. Warburton, and M. C. Löbl, Optically driving the radiative Auger transition, Nat. Commun. **12**, 6575 (2021).

[8] J. Yan, C. Chen, X.-D. Zhang, Y.-T. Wang, H.-G. Babin, A. D. Wieck, A. Ludwig, Y. Meng, X. Hu, H. Duan, W. Chen, W. Fang, M. Cygorek, X. Lin, D.-W. Wang, C.-Y. Jin, and F. Liu, Coherent control of a high-orbital hole in a semiconductor quantum dot, Nat. Nanotechnol. **18**, 1139 (2023).

[9] F. Bloch and P. A. Ross, Radiative Auger effect, Phys. Rev. **47**, 884 (1935).

[10] F. Bloch, Double electron transitions in x-ray spectra, Phys. Rev. **48**, 187 (1935).

[11] T. Åberg and J. Utriainen, Evidence for a "radiative Auger effect" in x-ray photon emission, Phys. Rev. Lett. **22**, 1346 (1969).

[12] T. Åberg, Theory of the radiative Auger effect, Phys. Rev. A **4**, 1735 (1971).

[13] F. V. Antolinez, F. T. Rabouw, A. A. Rossinelli, J. Cui, and D. J. Norris, Observation of electron shakeup in CdSe/CdS core/shell nanoplatelets, Nano Lett. **19**, 8495 (2019).

[14] J. Llusar and J. I. Climente, Nature and control of shakeup processes in colloidal nanoplatelets, ACS Photon. **7**, 3086 (2020).

[15] P. Lochner, A. Kurzmann, J. Kerski, P. Stegmann, J. König, A. D. Wieck, A. Ludwig, A. Lorke, and M. Geller, Real-time detection of single Auger recombination events in a self-assembled quantum dot, Nano Lett. **20**, 1631 (2020).

[16] H. Mannel, J. Kerski, P. Lochner, M. Zöllner, A. D. Wieck, A. Ludwig, A. Lorke, and M. Geller, Auger and spin dynamics in a self-assembled quantum dot, J. Appl. Phys. **134**, 154304 (2023).

[17] M. Gawełczyk, M. Syperek, A. Maryński, P. Mrowiński, Ł. Dusanowski, K. Gawarecki, J. Misiewicz, A. Somers, J. P. Reithmaier, S. Höfling, and G. Sek, Exciton lifetime and emission polarization dispersion in strongly in-plane asymmetric nanostructures, Phys. Rev. B **96**, 245425 (2017).

[18] M. Holtkemper, D. E. Reiter, and T. Kuhn, Influence of the quantum dot geometry on p-shell transitions in differently charged quantum dots, Phys. Rev. B **97**, 075308 (2018).

[19] D. Huber, B. U. Lehner, D. Csontosová, M. Reindl, S. Schuler, S. F. Covre da Silva, P. Klenovský, and A. Rastelli, Single-particle-picture breakdown in laterally weakly confining GaAs quantum dots, Phys. Rev. B **100**, 235425 (2019).

[20] M. Zieliński, Fine structure of dark and bright excitons in vertical electric fields: Atomistic theory of alloyed self-assembled InGaAs quantum dots, Phys. Rev. B **102**, 245423 (2020).

[21] L. Jacak, P. Hawrylak, and A. Wojs, *Quantum Dots* (Springer Verlag, Berlin, 1998).

[22] P. Hawrylak, G. A. Narvaez, M. Bayer, and A. Forchel, Excitonic absorption in a quantum dot, Phys. Rev. Lett. **85**, 389 (2000).

[23] S. Raymond, S. Studenikin, A. Sachrajda, Z. Wasilewski, S. J. Cheng, W. Sheng, P. Hawrylak, A. Babinski, M. Potemski, G. Ortner, and M. Bayer, Excitonic energy shell structure of

self-assembled InGaAs/GaAs quantum dots, Phys. Rev. Lett. **92**, 187402 (2004).

[24] A. Wojs and P. Hawrylak, Negatively charged magnetoexcitons in quantum dots, Phys. Rev. B **51**, 10880 (1995).

[25] P. Hawrylak and M. Korkusiński, Electronic properties of self-assembled quantum dots, in *Single Quantum Dots, Fundamental Applications and New Concepts*, edited by P. Michler (Springer-Verlag, Berlin, 2003), pp. 25–92.

[26] M. Bayer, G. Ortner, O. Stern, A. Kuther, A. A. Gorbunov, A. Forchel, P. Hawrylak, S. Fafard, K. Hinzer, T. L. Reinecke, S. N. Walck, J. P. Reithmaier, F. Klopf, and F. Schäfer, Fine structure of neutral and charged excitons in self-assembled In(Ga)As/(Al)GaAs quantum dots, Phys. Rev. B **65**, 195315 (2002).

[27] P.-L. Ardelt, K. Gawarecki, K. Müller, A. M. Waeber, A. Bechtold, K. Oberhofer, J. M. Daniels, F. Klotz, M. Bichler, T. Kuhn, H. J. Krenner, P. Machnikowski, and J. J. Finley, Coulomb mediated hybridization of excitons in coupled quantum dots, Phys. Rev. Lett. **116**, 077401 (2016).

[28] Z. Wasilewski, S. Fafard, and J. McCaffrey, Size and shape engineering of vertically stacked self-assembled quantum dots, J. Cryst. Growth **201-202**, 1131 (1999).

[29] A. Ludwig, J. H. Prechtel, A. V. Kuhlmann, J. Houel, S. R. Valentin, R. J. Warburton, and A. D. Wieck, Ultra-low charge and spin noise in self-assembled quantum dots, J. Cryst. Growth **477**, 193 (2017).

[30] G. Bester and A. Zunger, Cylindrically shaped zinc-blende semiconductor quantum dots do not have cylindrical symmetry: Atomistic symmetry, atomic relaxation, and piezoelectric effects, Phys. Rev. B **71**, 045318 (2005).

[31] K. Gawarecki, Spin-orbit coupling and magnetic-field dependence of carrier states in a self-assembled quantum dot, Phys. Rev. B **97**, 235408 (2018).

[32] M. C. Löbl, S. Scholz, I. Söllner, J. Ritzmann, T. Denneulin, A. Kovács, B. E. Kardynał, A. D. Wieck, A. Ludwig, and R. J. Warburton, Excitons in InGaAs quantum dots without electron wetting layer states, Commun. Phys. **2**, 93 (2019).

[33] P. B. Joyce, T. J. Krzyewski, G. R. Bell, and T. S. Jones, Surface morphology evolution during the overgrowth of large InAs-GaAs quantum dots, Appl. Phys. Lett. **79**, 3615 (2001).

[34] S. Stobbe, T. W. Schlereth, S. Höfling, A. Forchel, J. M. Hvam, and P. Lodahl, Large quantum dots with small oscillator strength, Phys. Rev. B **82**, 233302 (2010).

[35] D. Mourad, A. Guille, T. Aubert, E. Brainis, and Z. Hens, Random-alloying induced signatures in the absorption spectra of colloidal quantum dots, Chem. Mater. **26**, 6852 (2014).

[36] K. Gawarecki and M. Zieliński, Importance of second-order deformation potentials in modeling of InAs/GaAs nanostructures, Phys. Rev. B **100**, 155409 (2019).

[37] J.-M. Jancu, R. Scholz, F. Beltram, and F. Bassani, Empirical spds* tight-binding calculation for cubic semiconductors: General method and material parameters, Phys. Rev. B **57**, 6493 (1998).

[38] C. Pryor, J. Kim, L. W. Wang, A. J. Williamson, and A. Zunger, Comparison of two methods for describing the strain profiles in quantum dots, J. Appl. Phys. **83**, 2548 (1998).

[39] G. Bester, X. Wu, D. Vanderbilt, and A. Zunger, Importance of second-order piezoelectric effects in zinc-blende semiconductors, Phys. Rev. Lett. **96**, 187602 (2006).

[40] S. Schulz, S. Schumacher, and G. Czycholl, Tight-binding model for semiconductor quantum dots with a wurtzite crystal structure: From one-particle properties to Coulomb correlations and optical spectra, Phys. Rev. B **73**, 245327 (2006).

[41] M. Zieliński, M. Korkusiński, and P. Hawrylak, Atomistic tight-binding theory of multiexciton complexes in a self-assembled InAs quantum dot, Phys. Rev. B **81**, 085301 (2010).

[42] M. Zieliński, W. Jaskólski, J. Aizpurua, and G. Bryant, Strain and spin-orbit effects in self-assembled quantum dots, Acta Phys. Pol. A **108**, 929 (2005).

[43] N. Bart, C. Dangel, P. Zajac, N. Spitzer, J. Ritzmann, M. Schmidt, H. G. Babin, R. Schott, S. R. Valentin, S. Scholz, Y. Wang, R. Uppu, D. Najer, M. C. Löbl, N. Tomm, A. Javadi, N. O. Antoniadis, L. Midolo, K. Müller, R. J. Warburton *et al.*, Wafer-scale epitaxial modulation of quantum dot density, Nat. Commun. **13**, 1633 (2022).

[44] M. Graf and P. Vogl, Electromagnetic fields and dielectric response in empirical tight-binding theory, Phys. Rev. B **51**, 4940 (1995).

[45] T. B. Boykin and P. Vogl, Dielectric response of molecules in empirical tight-binding theory, Phys. Rev. B **65**, 035202 (2001).

[46] K. Gawarecki and M. Zieliński, Electron g-factor in nanostructures: Continuum media and atomistic approach, Sci. Rep. **10**, 22001 (2020).

[47] C. J. Bradley and A. P. Cracknell, *The Mathematical Theory of Symmetry in Solids: Representation Theory for Point Groups and Space Groups* (Oxford, England, 1972).

[48] M. Zieliński, Y. Don, and D. Gershoni, Atomistic theory of dark excitons in self-assembled quantum dots of reduced symmetry, Phys. Rev. B **91**, 085403 (2015).

[49] A. Jain, O. Voznyy, S. Hoogland, M. Korkusinski, P. Hawrylak, and E. H. Sargent, Atomistic design of CdSe/CdS core–shell quantum dots with suppressed Auger recombination, Nano Lett. **16**, 6491 (2016).

[50] http://wcss.pl.

[51] T. Eissfeller, Theory of the electronic structure of quantum dots in external fields, Ph.D. thesis, Technical University of Munich, 2012.

[52] M. A. Caro, S. Schulz, and E. P. O'Reilly, Origin of nonlinear piezoelectricity in III-V semiconductors: Internal strain and bond ionicity from hybrid-functional density functional theory, Phys. Rev. B **91**, 075203 (2015).

[53] S. Adachi, Material parameters of $In_{1-x} Ga_x As_y P_{1-y}$ and related binaries, J. Appl. Phys. **53**, 8775 (1982).

[54] J. S. Blakemore, Semiconducting and other major properties of gallium arsenide, J. Appl. Phys. **53**, R123 (1982).

[55] C. E. Pryor and M.-E. Pistol, Atomistic $k \cdot p$ theory, J. Appl. Phys. **118**, 225702 (2015).

[56] S. Balay, S. Abhyankar, M. F. Adams, S. Benson, J. Brown, P. Brune, K. Buschelman, E. M. Constantinescu, L. Dalcin, A. Dener, V. Eijkhout, J. Faibussowitsch, W. D. Gropp, V. Hapla, T. Isaac, P. Jolivet, D. Karpeev, D. Kaushik, M. G. Knepley, F. Kong *et al.*, PETSc Web Page (2023), https://petsc.org/.

[57] S. Lee, L. Jönsson, J. W. Wilkins, G. W. Bryant, and G. Klimeck, Electron-hole correlations in semiconductor quantum dots with tight-binding wave functions, Phys. Rev. B **63**, 195318 (2001).

[58] P. T. Różański and M. Zieliński, Linear scaling approach for atomistic calculation of excitonic properties of 10-million-atom nanostructures, Phys. Rev. B **94**, 045440 (2016).

[59] A. Franceschetti, L. W. Wang, H. Fu, and A. Zunger, Short-range versus long-range electron-hole exchange interactions in semiconductor quantum dots, Phys. Rev. B **58**, R13367(R) (1998).

[60] J.-W. Luo, A. Franceschetti, and A. Zunger, Direct-bandgap InAs quantum-dots have long-range electron-hole exchange whereas indirect gap Si dots have short-range exchange, Nano Lett. **9**, 2648 (2009).

[61] M. Zieliński, Valence band offset, strain and shape effects on confined states in self-assembled InAs/InP and InAs/GaAs quantum dots, J. Phys.: Condens. Matter **25**, 465301 (2013).

[62] A. H. Barnett, J. Magland, and L. af Klinteberg, A parallel nonuniform fast Fourier transform library based on an "exponential of semicircle" kernel, SIAM J. Sci. Comput. **41**, C479 (2019).

[63] A. H. Barnett, Aliasing error of the $\exp(\beta\sqrt{1 - z^2})$ kernel in the nonuniform fast Fourier transform, Appl. Comput. Harmon. Anal. **51**, 1 (2021).

[64] J.-Y. Lee and L. Greengard, The type 3 nonuniform FFT and its applications, J. Comput. Phys. **206**, 1 (2005).